ORIGINAL RESEARCH

Electrospun Scaffold with Sustained Antibacterial and Tissue-Matched Mechanical Properties for Potential Application as Functional Mesh

Zhengni Liu
Xiaoqiang Zhu
Rui Tang [ORCID]

Department of Hernia and Abdominal Wall Surgery, Shanghai East Hospital, Tongji University, Shanghai, People's Republic of China

Introduction: Various materials and approaches have been used to reduce the mesh-induced inflammatory response and modify the mesh with tissue-matched mechanical properties, aiming to improve the repair of abdominal wall defects.

Materials and Methods: In this study, we fabricated a polycaprolactone (PCL)/silk fibroin (SF) mesh integrated with amoxicillin (AMX)-incorporating multiwalled carbon nanotubes (MWCNTs) via electrospinning, grafting and crosslinking, developing a sustainable antibiotic and flexible mesh. AMX was loaded into the hollow tubular MWCNTs by physical adsorption, and a nanofibrous structure was constructed by electrospinning PCL and SF (40:60 w/w). The AMX@MWCNTs were then chemically grafted onto the surfaces of the PCL/SF nanofibers by treating with 1-ethyl-3-(3-dimethyl aminopropyl) carbodiimide/ *N*-hydroxysuccinimide (EDC/NHS) solution for simultaneous crosslinking and coating. The incorporation of AMX into the MWCNTs (AMX@MWCNTs) and the integration of the AMX@MWCNTs with the PCL/SF nanofibers were characterized. Then, the functional mesh was fabricated and fully evaluated in terms of antibacterial activity, mechanical properties and host response.

Results: Our results demonstrated that the PCL/SF nanofibrous structure was fabricated successfully by electrospinning. After integrating with AMX@MWCNT by grafting and crosslinking, the functional mesh showed undeformed structure, modified surface hydrophilicity and biocompatible interfaces, abdominal wall-matched mechanical properties, and a sustained-release antibiotic profile in *E. coli* growth inhibition compared to those of PCL/SF mesh in vitro. In a rat model with subcutaneous implantation, the functional mesh incited less mesh-induced inflammatory and foreign body responses than PCL/SF mesh within 14 days. The histological analysis revealed less infiltration of granulocytes and macrophages during this period, resulting in the loosely packed collagen deposition on the functional mesh and prominent collagen incorporation.

Discussion: Therefore, this designed PCL/SF–AMX@MWCNT nanofibrous mesh, functionalized with antibacterial and tissue-matched mechanical properties, provides a promising alternative for the repair of abdominal wall defects.

Keywords: functional mesh, antibacterial activity, sustained release, tissue-matched mechanical properties, electrospinning

Correspondence: Rui Tang
Department of Hernia and Abdominal Wall Surgery, Shanghai East Hospital, Tongji University, Shanghai, People's Republic of China
Email kevintown1972@126.com

Introduction

Clinical meshes available for abdominal wall defect repair can trigger an inflammatory response, infection, and even resulting in mesh explantation.[1] Other than prophylactic administration of antibiotics systematically, increasing attention has

been paid to optimizing meshes by reducing mesh-related inflammation for improving the outcome of such repairs.[2] The development of a functional mesh with antibacterial and anti-inflammatory properties is a clinically feasible strategy. The functionalization of such meshes is commonly achieved by equipping the mesh with agents such as antibiotics, antiseptics, or therapeutic genes to improve their biocompatibility, or by modifying their bioactivity.[3] Although promising results have been reported, these meshes have fallen far short on degradation, targeting, safety, cost, and handling, compromising their clinical applicability.[4] Moreover, because currently used meshes either degrade slowly or do not degrade to provide sufficient mechanical support, they are stiff in polymeric structures, which will be sharpened after functionalization, impairing the mechanical behavior and cause abdominal discomfort clinically. Therefore, the mechanical properties of the mesh are supposed to match with the compliance of native tissue to modulate the intra-abdominal pressure (IAP) dynamically.

Electrospinning is a versatile approach to constructing nano/microscale structures with unique properties for tissue engineering. Porous three-dimensional nanofibrous structures prepared by electrospinning are usually biodegradable with a high surface area, and can mimic the natural extracellular matrix (ECM) to provide a template for cell infiltration and tissue regeneration.[5] As one of the widely used polymers, PCL is an efficient electrospun template owing to its physicochemical and mechanical superiorities in tissue remodeling and regeneration. While SF is a cell-friendly biopolymer with numerous amino acids that act as pre-activated sites on its surface, and it can be used to functionalize the characteristics of the electrospun fiber by loading and releasing therapeutic agents.[6] In this scenario, we aim to combine these properties in a nanofibrous structure by electrospinning PCL with SF proportionally to fabricate a novel mesh. After grafting and crosslinking, the mesh is functionalized with antibiotics and with mechanical properties that match those of the native abdominal wall, aiming to facilitate the repair of abdominal wall defects.

The typical broad-spectrum antibiotic amoxicillin (AMX) has pronounced antibacterial effects. It could protect the meshes from *E. coli* contamination and inhibit mesh-related inflammation.[7] However, traditional drug loading methods, such as physical soaking or coating for the direct adsorption, are likely to cause its burst release and fail to maintain effective blood drug concentrations, which are essential to diminish the inflammation

throughout the integration and degradation of mesh.[8] Physical coating of antibiotics in polymeric mesh allows for sustained release of drugs. But the deposition of coatings over the mesh, either on the surface or in the inter-fiber spaces, alters its structure obviously.[9] Comparatively, chemical grafting is a more stable method to functionalized meshes with the antibacterial feature. Multiwalled carbon nanotubes (MWCNTs) have hollow tubular structures with inherent biocompatibility, a high specific surface area, and modifiable active groups that can function as inorganic and metabolizable therapeutic carriers.[10] We previously combined biodegradable plasma coating with physical adsorption to incorporate vascular endothelial growth factor (VEGF) into MWCNTs and achieved VEGF release from a biomaterial effectively.[11] Hence, the tubular structure of MWCNTs, with various integration sites on them, can be used to modify the AMX loading and sustained release at the desired level.

In this study, we fabricated a functional mesh that provides sustained antibiosis and native abdominal wall-matched mechanical properties. We used 1-ethyl-3-(3-dimethyl aminopropyl) carbodiimide (EDC)/ N-hydroxysuccinimide (NHS) solution to activate these grafting sites on PCL/SF and AMX-loaded MWCNT, and integrated them as a multigradient drug loading system, in which the nanofibers and MWCNTs acted as both drug containers and barriers for AMX releasing (Figure 1). The MWCNT-grafted nanofibers were the primary drug-release structure, and the AMX-loaded MWCNTs were the secondary release structure. We characterized the structural design of the mesh comprehensively, analyzed the sustained release of AMX and evaluated its mechanical properties in vitro. This functional mesh was applied to relieve the mesh-induced host response including inflammatory and immune response after subcutaneous implantation in a rat model, and provide evidence for potential abdominal wall defect repair.

Materials and Methods
Materials
PCL (M_w 80,000) was obtained from Sigma-Aldrich (Shanghai, China). SF was extracted from *Bombyx mori* silkworms (Second Silk Company, Zhejiang, China) by our group. AMX (>98%) and MWCNTs were purchased from Adamas (Emeryville, CA, USA) and Aladdin Industrial Company (China), respectively. The carboxylated MWCNTs with lengths of 10–30 μm had inner and outer diameters of approximately 5 and 20 nm, respectively. Hexafluoroisopropanol
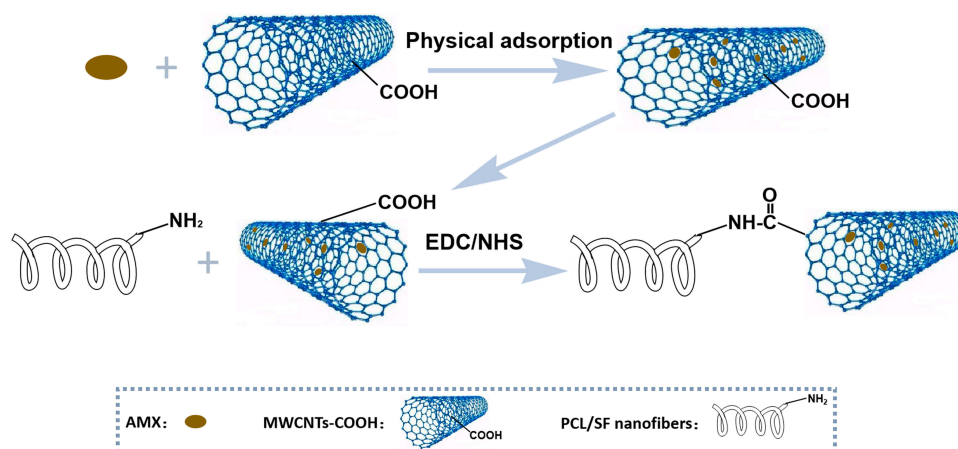
Figure 1 Schematic illustration of the preparation of PCL/SF-AMX@MWCNTs nanofibers.

(HFIP), EDC, and NHS were purchased from Sigma-Aldrich (St. Louis, MO, USA). *Escherichia coli* was purchased from Shanghai Fuzhong Biotechnology Development Co., Ltd. (Shanghai, China). Luria–Bertani (LB) medium was obtained from Sangon Biotech Co., Ltd. (Shanghai, China). L929 cells were obtained from the Institute of Biochemistry and Cell Biology (The Chinese Academy of Sciences, Shanghai, China). Dulbecco's modified Eagle's medium, fetal bovine serum, and glutaraldehyde were purchased from Shanghai Limin Industrial Co., Ltd. (Shanghai, China). Mouse polyclonal anti-CD11b and anti-CD68 antibodies were obtained from Santa Cruz Biotechnology, Inc. (Dallas, TX). Rabbit anti-collagen I antibody was purchased from Sigma-Aldrich (St. Louis, MO).

AMX Loading

To load MWCNTs with AMX, MWCNTs (30 mg) were added to aqueous AMX solution (1 mg/mL, 20 mL) containing methanol (2 mL). The mixture was ultrasonicated for 2 h and stirred at room temperature for another 24 h. The excess free AMX was removed from the mixture by centrifugation, and the pellet was washed three times with deionized water. The AMX remaining in the supernatant was analyzed with a Lambda 25 UV–vis spectrophotometer (Perkin Elmer, USA) at a wavelength of 228 nm. The AMX loading efficiency was calculated by

$$W(\%) = M_A/M_{tot} \times 100\% \qquad (1)$$

where W is the percentage AMX loading, M_A is the mass of adsorbed AMX, and M_{tot} is the mass of AMX@MWCNTs.

Functional Mesh Preparation

PCL and SF were dissolved in HFIP at an optimal concentration of 6%, and the PCL/SF weight ratio was 40:60. Electrospinning was performed with a steel capillary tube, with a 1.5mm-inner diameter tip mounted on an adjustable, electrically insulated stand. The composite PCL/SF nanofibers were prepared at a constant flow rate of 1.2 mL/h, a voltage of 10 kV, and the distance of 15 cm between the syringe pump and collector. After electrospinning, the PCL/SF nanofibers were collected with a paperboard wrapped with aluminum foil and vacuum dried for 48 h.

Then the PCL/SF nanofibers were coated with AMX@MWCNTs through an amidation reaction using EDC/NHS solution. EDC (2.15 g) and NHS (0.69 g) were dissolved in 95% ethanol (100 mL) containing AMX@MWCNTs (20 mg) and stirred for 30 min. The dried PCL/SF nanofibrous mesh (5.0 × 5.0 cm²) was immersed in the EDC/NHS/AMX@MWCNT crosslinking solution for 3 h, and then washed three times with distilled water. The PCL/SF–AMX@MWCNT nanofibrous mesh was lyophilized for 48 h.

Characterization of Functional Meshes

The morphological structures of the meshes were investigated with scanning electron microscopy (SEM; Phenom XL, Phenom, Netherlands) at an accelerated voltage of 10 kV after sputter-coated with platinum (8 mA, 45s). The collected images were used to measure the fiber diameters, pore sizes, and porosity with the ImageJ software (NIH, Bethesda, MD, USA). The water contact angles of the meshes were analyzed with a contact angle instrument (OCA40, DataPhysics, Germany). Each sample was measured three times for

calculating the average results. The inner structure of AMX@MWCNTs was observed by transmission electron microscopy (TEM; JEOL, JEM-2100, Japan) at 200 kV to confirm the loading of AMX. The Fourier transform infrared (FTIR) spectroscopy (Thermo Fisher, Nicolet Nexus 670, USA) was performed to determine the characteristic bands of AMX, PCL/SF nanofibers and PCL/SF–AMX@MWCNT nanofibers.

Mechanical Properties

The mechanical properties of these meshes, namely, the stress-strain curve, tensile strength, elongation at break, Young's moduli and the cyclic compression curve at 50% deformation, were measured with a mechanical testing system (HY-940FS, Shanghai Hengyu Instrument Co., Ltd., China). The samples were cut into 50×10 mm^2 strips (n = 5) and immersed in phosphate-buffered saline (PBS) for 2 h to maintain their wettability before testing. Samples 10 mm long were set between two grippers, which were gradually moved apart at a rate of 2 mm/min with a load of 100 N until complete rupture. The tensile strength was calculated as the maximal load divided by the cross-sectional area (MPa). Elongation data represents that the sample tolerates an increased stretch before breakage and Young's modulus (MPa) was calculated from the linear slope of the stress−strain curve. The cyclic tensile tests were repeated for five cycles at a rate of 2 mm/min to demonstrate the deforming extent of samples under stretched condition. All the tests were performed at room temperature.

AMX Release and Antibacterial Activity

The release kinetics of AMX from the AMX@MWCNTs and PCL/SF–AMX@MWCNT meshes were analyzed with a UV–vis spectrophotometer (Lambda 25, Perkin Elmer, USA). In brief, AMX@MWCNTs (2 mg) were suspended in PBS (3 mL, pH=7.4) in a dialysis bag (M_w=3500 Da). The dialysis bag was placed in a centrifuge tube with PBS (50 mL). PCL/SF–AMX@MWCNT meshes were treated similarly to make the amount of AMX equal to that in the AMX@MWCNTs. The samples were shaken at 90 rpm at 37 °C in a table concentrator. A sample of the supernatant (3 mL) was collected at various times to detect the absorbance of AMX at 228 nm with same volume of PBS replenished. The amount of AMX released from the mixture was divided by the total integrated amount of AMX to calculate the cumulative release rates (%) of AMX at different intervals.

Accordingly, the drug release kinetics of AMX@MWCNTs and PCL/SF–AMX@MWCNT were plotted, respectively.

The Gram-negative bacterium *E. coli* was used as the model bacterium for antibacterial activity test. For quantitative analysis, *E. coli* was activated in fresh LB medium and slowly shaken in an incubator (80 rpm) at 37 °C. AMX@MWCNTs (10 mL) with different concentrations of AMX (0, 20, 40, or 60 μg/mL) were incubated in a tube and then the bacterial culture (1 mL, 1×10^8 CFU/mL) was added to the tube. The culture was incubated in the table concentrator at a rotational speed of 100 rpm for 24 h. The absorbances of the bacterial cultures were measured at a wavelength of 600 nm and the percentage bacterial inhibition was calculated as

$$bacterial\ inhibition\ (\%) = (OD_c - OD_s)/OD_c \times 100\% \tag{2}$$

where OD_c is the absorbance of the control and OD_s is the absorbance of the sample.

The antibacterial activities of the AMX-loaded meshes were also determined. The round-shaped PCL/SF, PCL/SF/AMX and PCL/SF-AMX@MWCNTs (1.0×1.0 cm^2) were fixed on the surface of LB medium, and overlaid with *E. coli*. The bacteria were cultured at 37 °C for 24 h, and then the diameter of the ring of bacterial inhibition was measured to evaluate the antibacterial activities of the AMX-loaded nanofiber meshes qualitatively.

Biocompatibility

The biocompatibility of the AMX-loaded meshes was analyzed with a cell proliferation assay in vitro. Both PCL/SF mesh and PCL/SF–-AMX@MWCNT mesh were cut into small round pieces (14 mm diameter), placed in a 24-well plate, and sterilized for 2 h by immersing in 75% ethanol. Mouse fibroblast cells (L929) were seeded on the surfaces of the meshes at a density of 1.5×10^4 cells/well. Cells seeded on coverslips were used as the control.

The viability of the L929 cells was evaluated with a Cell Counting Kit-8 assay [CCK-8, Dojindo, Kumamoto, Japan) after culturing for 1, 3, or 5 days and measured three times to calculate the average results and standard deviations. The morphology of the cells on the surfaces of the meshes was observed by SEM on the third day. The nuclei and cytoskeletons of the L929 cells were stained with 4′,6′-diamidino-2-phenylindole hydrochloride (DAPI; Invitrogen, USA) and fluorescein isothiocyanate (FITC)-conjugated phalloidin (Invitrogen), respectively. The attachment and proliferation of the cells were observed with a fluorescence microscope

(TS100, Nikon, Japan). The cell-producing collagen I were immunostained with DAPI and anti-Collagen I (1:100; Sigma) and observed by confocal laser scanning microscopy (LSM 710, Carl Zeiss GmbH).

Subcutaneous Implantation and Histological Analysis

Twelve male Sprague Dawley rats, weighing approximately 250 g, were obtained from SLAC National Rodent Laboratory Animal Resources (Shanghai, China). The meshes were subcutaneously implanted into the backs of the rats to evaluate its host response. The Institutional Review Committee of Tongji University School of Medicine (Shanghai, China) approved all animal study protocols based upon the 3Rs policy (replacement, reduction, and refinement). The meshes were implanted as follows. The rats were randomly assigned to the PCL/SF group or the PCL/SF–AMX@MWCNT group. Under anesthesia induced by an intraperitoneal injection of pentobarbital (0.1mg/g), the rats were shaved around the implantation area. A skin incision (1 cm in length) was made in the dorsal midline, and the sterilized mesh ($8 \times 8 \times 2$ mm^3) was implanted into the subcutaneous pocket. The skin was closed with 5–0 Vicryl interrupted sutures (Ethicon).

After surgery, the rats were housed according to the standards of the National Institutes of Health Guide for the Care and Use of Laboratory Animals (NIH publication N01-OD -4-2139, Revision 2). No antibiotic prophylaxis was administered after surgery. The rats were killed randomly 7 or 14 days after surgery with an intravenous injection of thiopental. The implanted materials were retrieved together with the surrounding tissues and prepared for paraffin embedding. The samples were sectioned to 3.5 μm and stained with hematoxylin and eosin (H&E), Masson's trichrome staining. The host inflammatory and immune responses, represented by granulocytes and macrophage infiltration, were evaluated by immunohistochemical staining with anti-CD11b (diluted 1:200; Santa Cruz Biotechnology) and anti-CD68 antibodies (diluted 1:200; Santa Cruz Biotechnology), respectively. The inflammation-reacted collagen deposition on the mesh was also stained with anti-Collagen I (1:100; Sigma) immunohistochemically. The images were collected, and the data were analyzed by two blinded investigators with ImageJ software (NIH, Bethesda, MD).

Statistical Analysis

Continuous variables are presented as mean ± standard deviation and analyzed with two-tailed Student's *t*-test or one-way analysis of variance followed by the Student −Newman−Keuls post hoc test. SPSS version 22.0 software (SPSS, Inc., Chicago, IL) was used for all statistical analyses. A *P* value of 0.05 was selected as the significance level (*$P < 0.05$ and **$P < 0.01$).

Results
Characterization of Functional Mesh

The morphologies and diameter distributions of the meshes were distinguished between PCL/SF and PCL/SF–AMX@MWCNTs (Figure 2). Before coating, the PCL/SF meshes exhibited a continuous intact nanofibrous structure with the fiber diameter of 250 ± 70 nm. In contrast, local and heterogeneous agglutination was visible on the surfaces of the PCL/SF–AMX@MWCNTs meshes after coating, with the fiber diameter decreased to 191 ± 42 nm ($P > 0.05$, Figure 2A–F). The pore size of PLC/SF increased slightly after the integration of AMX@MWCNTs ($P > 0.05$, Figure 2G). The subtle difference in fiber diameter and pore size could be attributed to the partial dissolution of SF in the fibers and adsorption of the AMX@MWCNT activator in the fiber pores during the grafting and crosslinking.[12] Meanwhile, the agglomeration of AMX@MWCNTs on the surface of PLC/ SF reduced its porosity slightly ($P > 0.05$, Figure 2H). The result of wettability demonstrated the intrinsic hydrophilicity of PCL/SF was further enhanced by integrating AMX@MWCNTs (Figure 2I and J), which reduced the water contact angle from 69° ± 5° to 56° ± 3° ($P < 0.05$). The exposure of some hydrophilic groups and the increase in the pore size during the process may play a decisive role in the hydrophilicity modification.[13]

TEM images of the MWCNTs after AMX loading (Figure 3A) showed that AMX (red arrows in Figure 3B) was incorporated into the MWCNTs and dispersed in the tube with no structural deformation. FTIR spectra also confirmed the grafting of AMX@MWCNT on the PCL/ SF meshes. The spectrum of AMX showed the peak at 3181 cm^{-1} that represents the stretching vibration of the hydroxyl group in the AMX structure, and the sharp peaks at 1689 and 1519 cm^{-1} arise from amides I and II in AMX, respectively (Figure 3C).[14] Other characteristic peaks at 1770, 1608, and 1018 cm^{-1} are attributed to the stretching vibration of C=O, the stretching vibration of the benzene ring, and C–S, respectively. In the spectra of PCL/SF based meshes, some characteristic peaks of PCL/SF– AMX@MWCNTs were stronger than those of PCL/SF, and such peak shifted from 1727 cm^{-1} to 1631 cm^{-1}
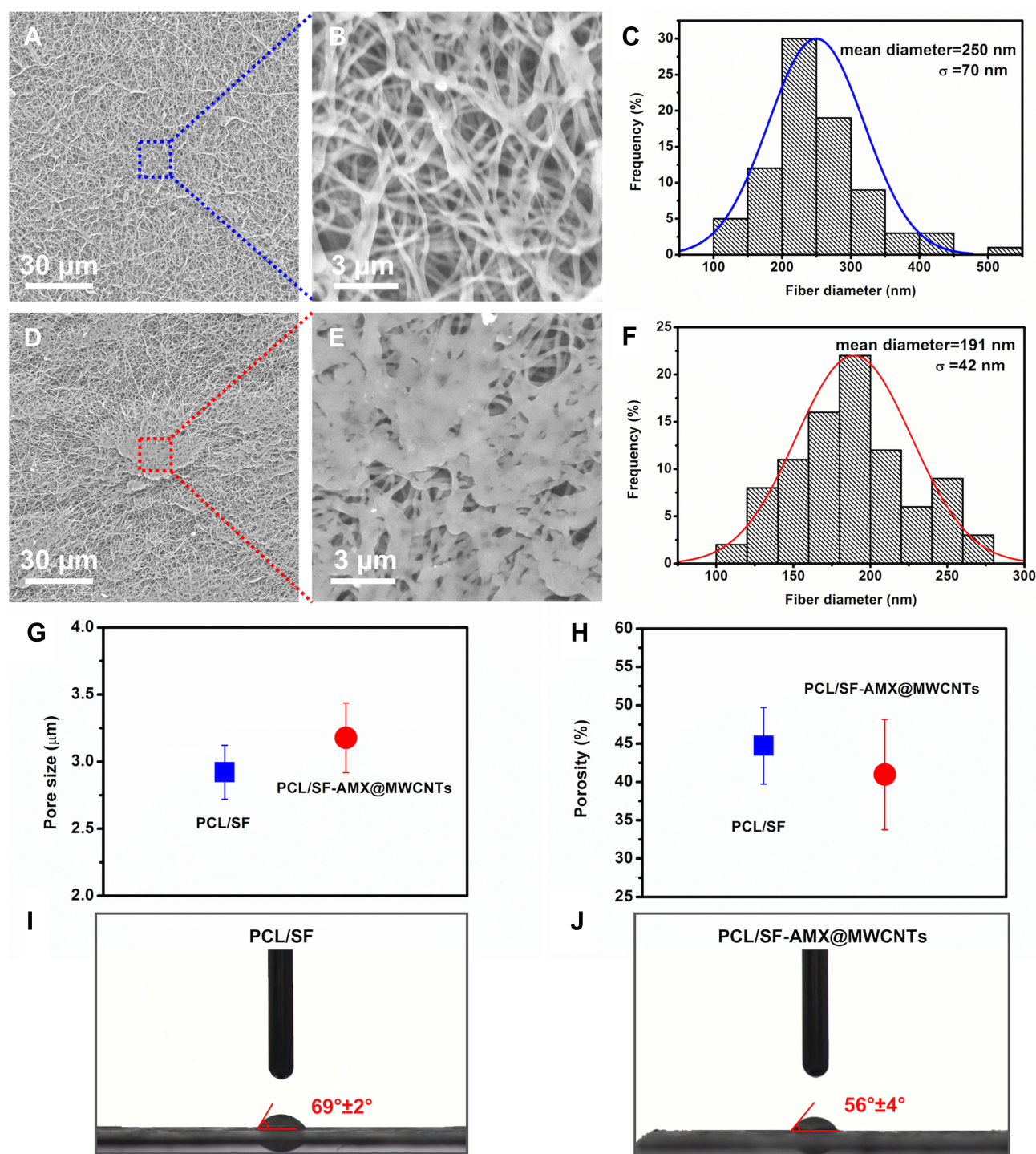
Figure 2 Representative SEM images of PCL/SF nanofibers and the corresponding diameter distributions (**A–C**), Representative SEM images of PCL/SF–AMX@MWCNT nanofibers and its diameter distributions (**D–F**). Pore size (**G**), porosity (**H**) of the water contact angles (**I** and **J**) of PCL/SF mesh and PCL/SF–AMX@MWCNT mesh.

after crosslinking and coating. More importantly, we confirmed the loading of AMX by detecting the optimal characteristic peak of AMX at 3289 cm^{-1} in PCL/SF–AMX@MWCNTs (Figure 3D).

Mechanical Properties

The representative mechanical properties of the meshes, including tensile stress–strain curves, tensile strength, elongation and Young's modulus, which depend on the mesh
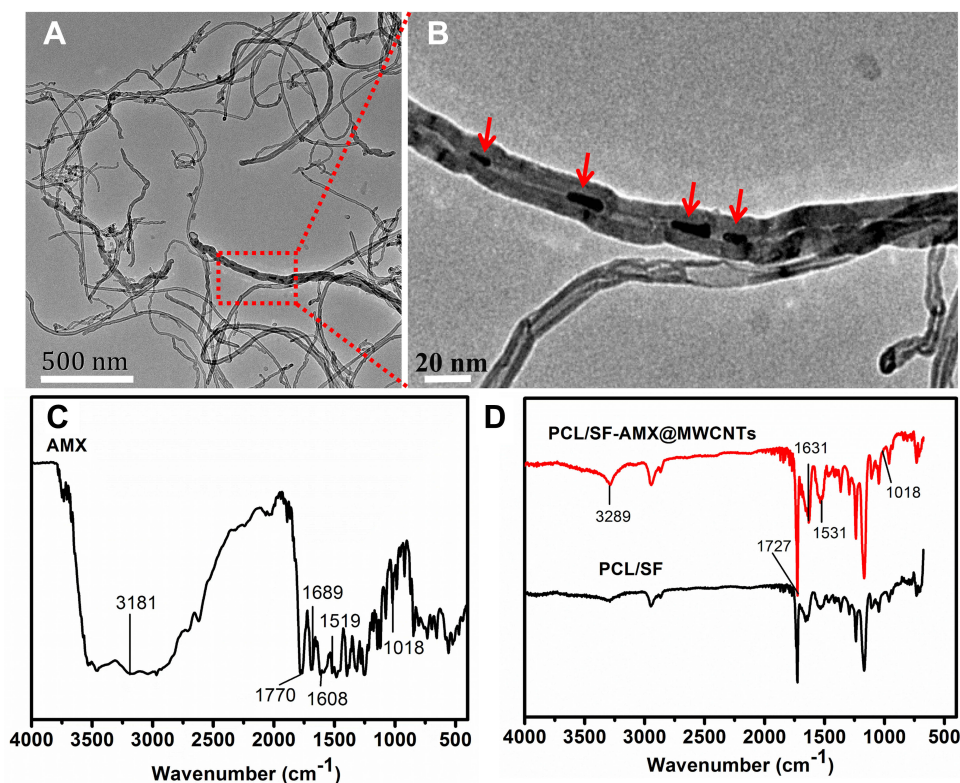
Figure 3 TEM images of AMX@MWCNT particles (**A** and **B**); FTIR spectra of AMX (**C**), PCL/SF and PCL/SF–AMX@MWCNT (**D**). Red arrows indicate AMX in (**B**).

components and structures, were analyzed comparatively. The strain-stress curves of the meshes showed that PCL/SF turned to be more elastic and less strengthening after integrating AMX@MWCNTs (Figure 4A). The comparison revealed that the tensile strength of the PCL/SF meshes decreased from 3.97 ± 0.92 to 3.08 ± 0.43 MPa after integration (Figure 4B, $P > 0.05$). The elongation of the PCL/SF

mesh at breaking was $60 \pm 12\%$, whereas the value of PCL/SF–AMX@MWCNT mesh stretched to approximately $150 \pm 11\%$ (Figure 4C, $P < 0.01$). Accordingly, we detected a reduction in Young's modulus from 8.08 ± 0.65 to 2.86 ± 0.20 MPa ($P < 0.01$, Figure 4D). The preconditional coatings on the meshes confirmed the inhibition of AMX@MWCNTs on molecular chains in the strength modification, but it
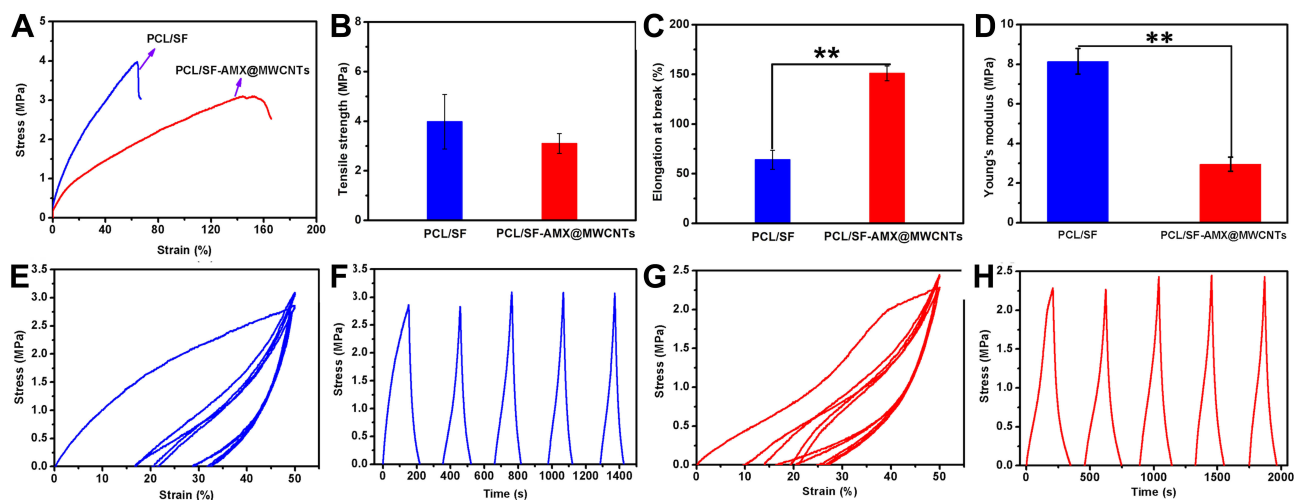

Figure 4 Representative mechanical properties of nanofibrous meshes. Stress-strain curves (**A**), tensile strength (**B**), elongation at break (**C**), Young's modulus (**D**), and cyclic tensile response curves at 50% deformation of PCL/SF mesh (**E** and **F**) and PCL/SF-AMX@MWCNTs mesh (**G** and **H**). **$P < 0.01$ in (**C**) and (**D**).

elasticized the nanofibrous structure with the concurrent crosslinking. It made the elongation at break of the PCL/SF-AMX@MWCNTs mesh close to the expansion of the native abdominal wall, which is approximately 112–127% in different stretch directions, and female even exhibits increased compliance compared to males in the cranio-caudal, medial-lateral and oblique directions.[15]

Further cyclic stretching was performed to evaluate the stability of such elasticity under wet conditions at a rate of 2 mm/min. The results indicated both the PCL/SF and PCL/SF–AMX@MWCNT meshes showed distinctive hysteresis loops in the first cycle. The strain loss of the PCL/SF–AMX@MWCNT mesh was about 10% in the first cycle, whereas that of the PCL/SF mesh was approximately 17% (Figure 4E–H). During stretching cycle, the PCL/SF–AMX@MWCNT mesh showed a smaller total strain loss, indicating the forming of the dense molecular prototype after functionalization increased the crystallinity of the mesh, and stabilized it by reducing the fracture rate of the local macromolecular chains.

AMX Release and Antibacterial Activity

In vitro release kinetics of AMX from AMX@MWCNTs and PCL/SF–AMX@MWCNTs were explored for 72 h (Figure 5A). The results demonstrated AMX in PCL/SF–AMX@MWCNTs released more slowly than that in AMX@MWCNTs after the initial burst release in both. After 72 h, the cumulative release of AMX from the PCL/SF–AMX@MWCNT was 11%, whereas that from AMX@MWCNTs reached 34.7% ($P < 0.05$). It indicated that the PCL/SF–AMX@MWCNT mesh, with a multigradient release structure, exhibited sustained AMX release. Drug release kinetics were described with a first-order kinetics equation, in which the goodness of fit (R^2) values were 0.982 and 0.933 for AMX@MWCNTs and PCL/SF–AMX@MWCNTs, respectively. The PCL/SF–AMX@MWCNTs presented a flatter release curve in a sustained manner via a typical Fickian diffusion mechanism (Figure 5B and C).

To evaluate the antibacterial activity of AMX-loaded MWCNTs, we calculated the inhibition of *E. coli* by escalating the concentrations of AMX in AMX@MWCNTs (Figure 5D). The result showed that the antibacterial efficacy of AMX@MWCNTs was improved from 25% to 80% ($P < 0.05$) by escalating AMX concentration, indicating a positive correlation between them. The loading efficiency of AMX in AMX@MWCNTs is 81.5 ± 2.3%. The converted values of PCL/SF and PCL/SF-AMX@MWCNT meshes are 5.2 ± 0.5 mg/cm^2 and 4.3 ± 0.7 mg/cm^2 ($P<0.05$, Figure 5E), which implies sufficient to prevent contamination in an infected animal model.[22] In the antibacterial activities test, bacterial inhibition rings formed
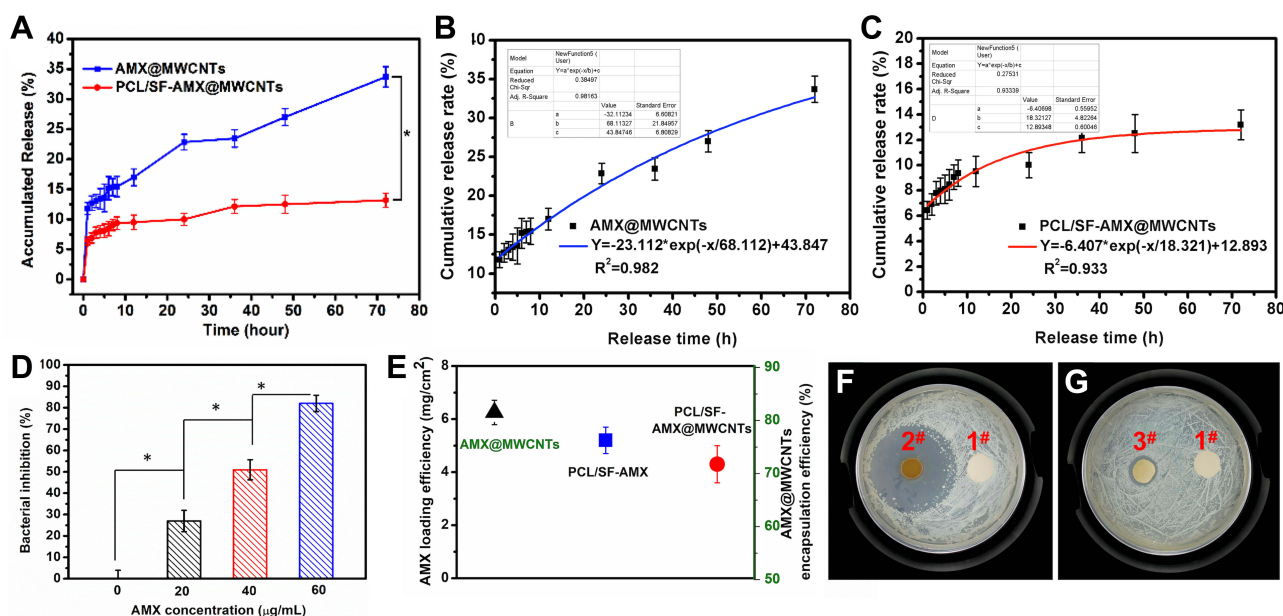

Figure 5 In vitro release of AMX from AMX@MWCNTs and PCL/SF–AMX@MWCNTs meshes for 72 h (**A**). First-order kinetics equation fitting for AMX@MWCNTs (**B**) and PCL/SF–AMX@MWCNTs (**C**). Bacterial inhibition of *E. coli* growth by AMX (%) at various concentrations after incubation for 24 h (**D**). The loading efficiency of AMX in AMX@MWCNT, PCL/SF and PCL/SF-AMX@MWCNT meshes (**E**). Growth inhibition of *E. coli* on agar plates cocultured with the PCL/SF/AMX mesh (**F**) and PCL/SF–AMX@MWCNT mesh (**G**) for 24 h. 1#, 2# and 3# indicate the PCL/SF mesh, PCL/SF–AMX mesh, and PCL/SF–AMX@MWCNT mesh, respectively. *$P < 0.05$ in (**A**) and (**D**).

around both the PCL/SF–AMX and PCL/SF–AMX@MWCNT meshes in response to the AMX present in them, whereas PCL/SF showed no antibacterial activity after culturing for 24 h (Figure 5F and G). Owing to the initial burst release of AMX, PCL/SF/AMX showed higher antibacterial activity than that of PCL/SF–AMX@MWCNT by forming bigger bacterial inhibition rings. The statistical differences were analyzed to reflect their various antibacterial manners (Table 1).

Biocompatibility

Before the potential utility of the functional mesh in vivo, the biocompatibility of PCL/SF and PCL/SF–AMX@MWCNTs was evaluated. It indicated that there was no statistical difference in cell viability on day 1 (Figure 6A). After culturing for 3 days, the cells on PCL/SF–AMX@MWCNTs obtained the highest absorbance value ($P < 0.05$), whereas the cells on PCL/SF and coverslips behaved similarly ($P > 0.05$). On day 5, both PCL/SF and PCL/SF-AMX@MWCNTs exceeded coverslips on proliferation ($P < 0.05$), and PCL/SF–AMX@MWCNTs obtained the highest value ($P < 0.01$). We inferred that the improved hydrophilicity of PCL/SF-AMX@MWCNTs promoted cell attachment and proliferation on the mesh.

Representative SEM images showed that L929 cells cultured on the nanofibrous meshes for 3 days were spindle-shaped with extended pseudopods, and were dispersed (Figure 6B). It indicated that the PCL/SF nanofibrous structure provided a biocompatible interface for cells attachment before and after the introduction of AMX@MWCNTs, confirming AMX@MWCNTs had little cytocompatibility. Furthermore, cytoskeletons of the cells and cell-secreted collagen I were visualized, respectively (Figure 6C). We observed the denser distribution of the mature cells and intensive expression of collagen I on the PCL/SF-AMX@MWCNT meshes. It also proved the

superior biocompatibility of the functional mesh facilitated cellular performances, which is consistent with the results of cell proliferation.

Histological Analysis in vivo

These host events were mainly the infiltration of neutrophils, lymphocytes, macrophages and typical collagen, fibronectin deposition following fibrous capsule formation. H&E-stained sections showed that both the PCL/SF and PCL/SF–AMX@MWCNT explants induced inflammatory cell infiltration and the formation of granulomatous tissue after 7 days (Figure 7A). At the interface between the mesh and the host tissue, more cell infiltration in compact matrixes were observed around the PCL/SF mesh, while fewer cell infiltration with loose fibrous tissue was detected in the inflamed area beneath the PCL/SF–AMX@MWCNT mesh. After implantation for 14 days, with the inflammatory response gradually subsided, the PCL/SF–AMX@MWCNT mesh presented a milder inflammatory response than PCL/SF mesh, with the formation of loose and disorganized connective tissue. Masson's trichrome stained sections highlighted fibrous capsules composed of collagen in blue. Capsule thickness was defined as the thickness of the collagen fibrous tissue extending from the basal side or apical side of the implant. The PCL/SF mesh induced thicker and more compact fibrous capsules than the PCL/SF–AMX@MWCNT mesh did at day 7 and 14 (Figure 7B, $P < 0.05$).

The inflammatory reaction was quantitatively analyzed by the expression of CD11b and CD68 to determine the degree of granulocytes and macrophages infiltrations into the meshes, respectively (Figure 7C–E). After 7 days, the immunostaining images of CD11b showed that the PCL/SF meshes were heavily infiltrated with granulocytes and reached a higher level than that of PCL/SF-AMX@MWCNTS meshes ($P < 0.05$). This inflammation substantially attenuated but maintained the difference of infiltration level between two groups after 14 days ($P < 0.05$). Similarly, the immunostaining for the characteristic expression of CD68 showed that PCL/SF meshes induced more intensive immunoreaction than PCL/SF-AMX@MWCNTs by macrophages recruitment and infiltration within 14 days ($P < 0.05$).

The overgrowth of inflammatory cells and collagen secretion is followed by excess deposition of ECM on the surface, instead of proper remodeling into the structure, causing adhesion and fibrous tissue encapsulation. In the immunohistochemical staining of collagen I, obvious newly formed collagen mainly deposited on both of the meshes

Table 1 Diameters of Bacterial Inhibition Rings Around the PCL/SF Mesh, PCL/SF–AMX Mesh, and PCL/SF–AMX@MWCNT Mesh After Coculture with *E. coli* for 24 h vs PCL/SF-AMX@MWCNTs

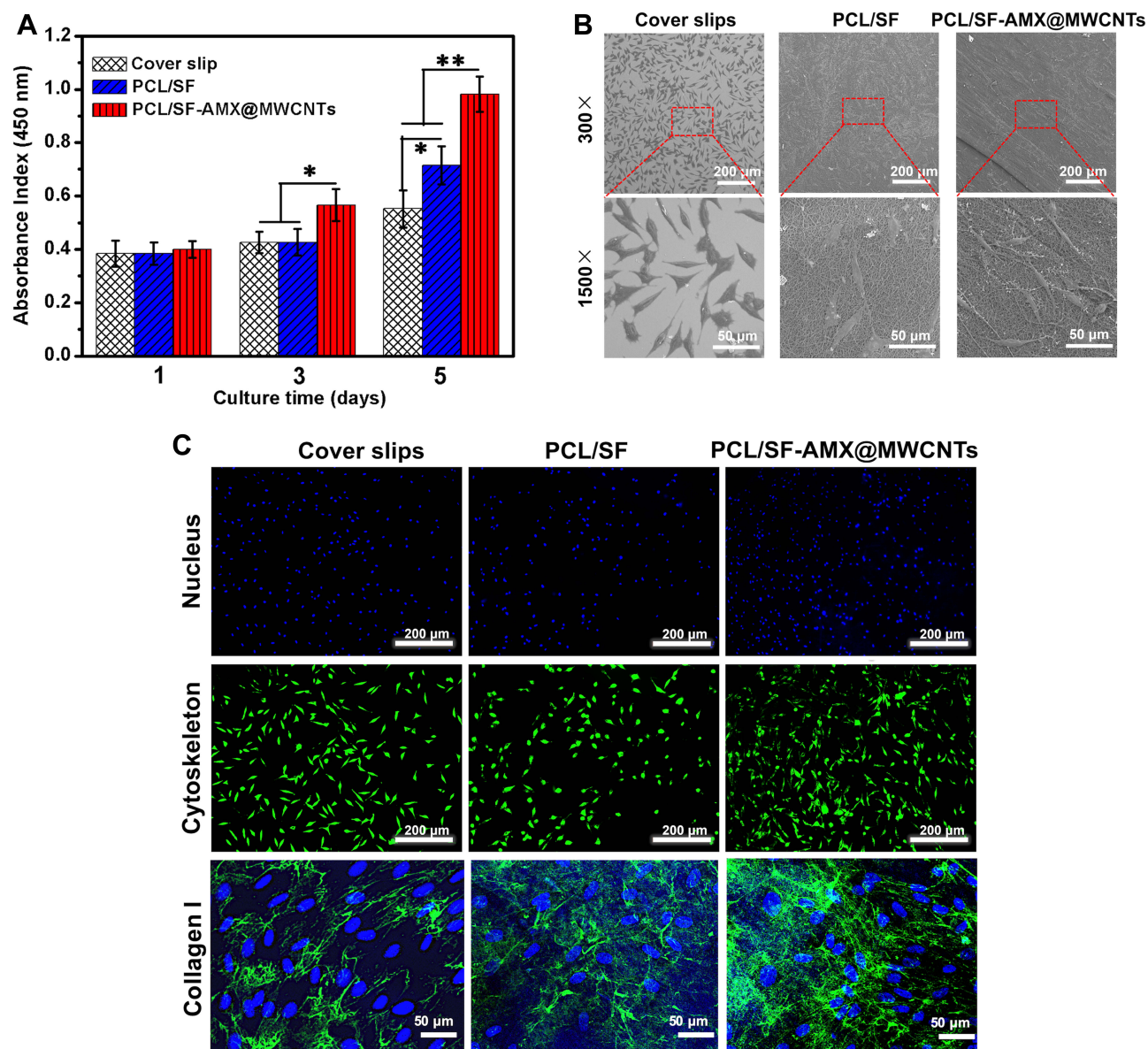| Samples	External Diameter (cm)	Inner Diameter (cm)	Diameter Difference (cm)
PCL/SF	–	–	–
PCL/SF–AMX	3.52 ± 0.02*	0.85 ± 0.12	2.67 ± 0.10*
PCL/SF–AMX@MWCNTs	1.29 ± 0.02	0.81 ± 0.09	0.48 ± 0.02

Note: *$P < 0.05$

Figure 6 The proliferation of L929 cells after culturing for 1, 3, and 5 days (**A**) and cell morphology on coverslips, PCL/SF mesh, and PCL/SF–AMX@MWCNT mesh after 3 days (**B**). FITC-conjugated phalloidin (green)/DAPI (blue) staining of cells, and collagen I (green) and DAPI (blue) staining of cells after culturing for 3 days on coverslips and various meshes accordingly (**C**). *P < 0.05 and **P < 0.01 in (**A**).

after 7 days. The fibrous capsule formed on different meshes could be distinguished by the border between the meshes and capsules (red dotted lines). After 14 days, denser packed of collagen deposited on PCL/SF meshes owing to its aggressive host responses. In contrast, loosely well-oriented fibrils formed on PCL/SF–AMX@MWCNT meshes with prominent collagen remodeling in it.

Discussion

Fabricating a biomimetic structure for tissue repair requires to integrate various components with diverse techniques

because the functional restoration of a native tissue is a complex process. Concerning the reconstruction of abdominal wall, mesh-induced responses and matching mechanical supports are essential for the process.[16] Electrospinning is a cost-effective way to optimize the structural and biocompatible features of different materials for biomedical applications. In these structures, several critical parameters including the fiber diameter, pore size, porosity, and water contact angle determine the engineered properties.[17] In the study, we characterized the functional meshes comparatively. Despite the mesh, after integrating AMX@MWCNT,
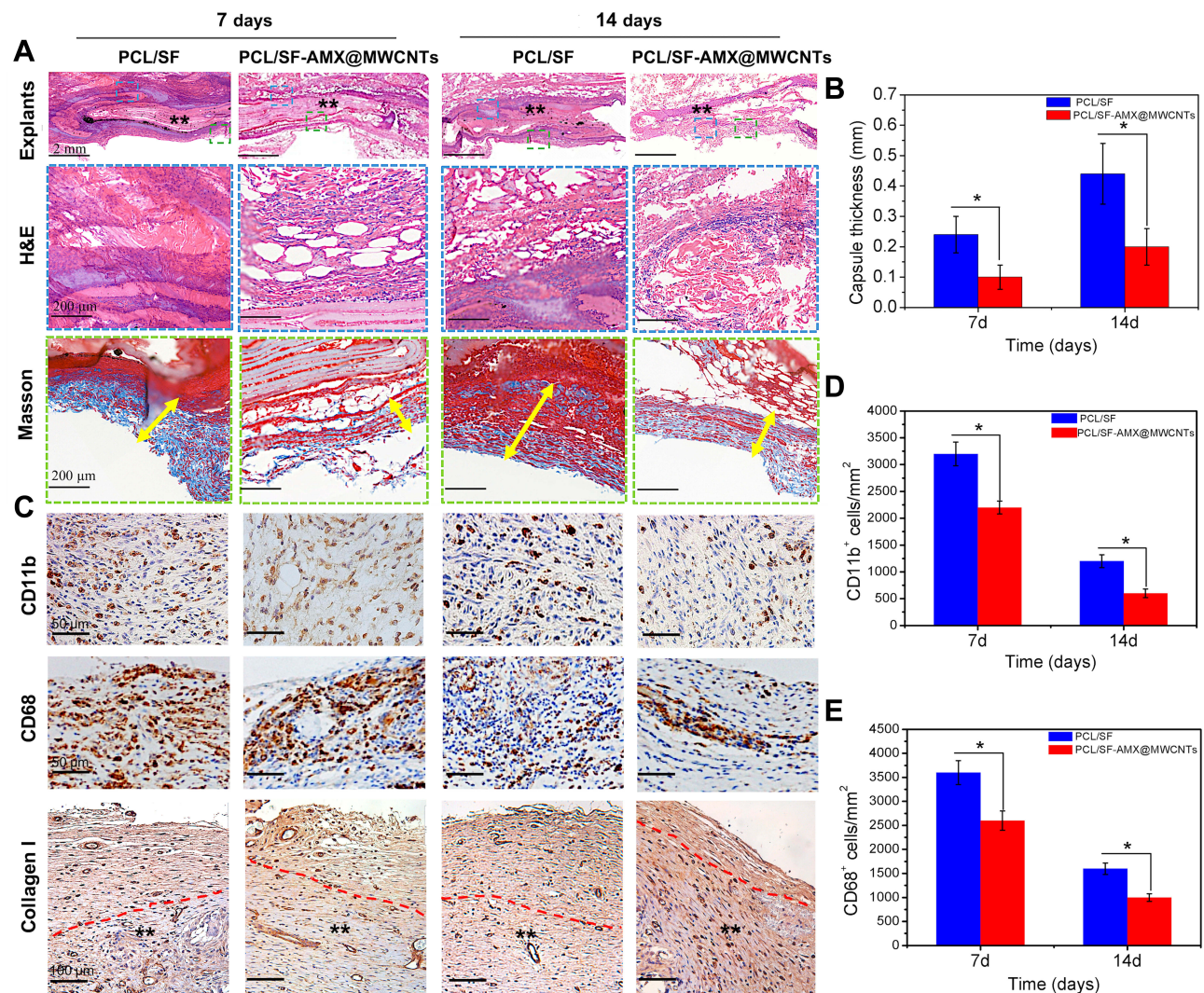
Figure 7 Histological analysis of PCL/SF mesh and PCL/SF–AMX@MWCNT mesh after their subcutaneous implantation in rats for 7 or 14 days (**A**). The scale bars in the explants, H&E and Masson rows of images indicate 2 mm, 200 μm and 200 μm. ** indicated meshes, and the yellow arrowed lines marked the capsule thickness in (**A**); The quantitative thickness of fibrous capsules (**B**); CD11b, CD68 and collagen I immunohistochemical staining (**C**); CD11b, CD68 and collagen I rows of images indicate 50 μm, 50 μm and 100 μm, respectively. **indicated meshes, and the red dotted lines marked the border between mesh and collagen deposition in (**C**); The quantification of CD11b (**D**) and CD68 (**E**) positive cells in the staining. *$P < 0.05$ in (**B**) and (**D** and **E**).

exhibited distinctive appearance locally, the statistical results of characterization proved their similar nanoscale structures. It revealed that the chemical grafting does not involve alteration of the bulk fibers in the structure but only the superficial molecular layers. Moreover, it improved the hydrophilicity of the PCL/SF–AMX@MWCNTs mesh by reducing the water contact angle, which also explains its superior biocompatibility by facilitating cell attachment, proliferation and secretion on mesh.[18]

The tensile strength of PCL/SF–AMX@MWCNT mesh decreased slightly after the introduction of AMX@MWCNTs. But it was sufficient for the repair of transversalis fascia (tensile strength=1.5MPa, elastic modulus=3.0MPa), which is a key tissue layer to be reinforced in inguinal herniation.[19] More importantly, the original elasticity of PCL/SF mesh was modified to match with that of the native abdominal wall. In mechanical modification, the surface grafting does not result in excessive agents deposition in the inter-fiber or space, but it is principally responsible for the stable and elastic structure by combining with the crosslinking treatment using EDC/NHS. In a clinical context, meshes with different geometries and made of different materials have varying degrees of anisotropy. However, synthetic meshes either be woven, knitted, or expanded polymer constructs, rarely adapt to the biomechanical features of the native abdominal wall in

some way.[20] The inflexibility of the implants with sudden soaring in IAP can cause postoperative pain and even repair rupture, whereas an overflexible mesh can cause a bulge or herniation at the repair site.[21] In some cases, when the mesh is implanted superficially, the stiff mesh may result in the foreign body sensation and irreversible activity-related pain for patients. Therefore, matching the elasticity of the mesh with the compliance of native abdominal wall is preconditional for the repair, so that it can modulate the fluctuant IAP dynamically and reduce the risk of related complications.

Mesh infection is a fatal complication occurring after mesh hernioplasty, which has to be removed in some cases of deep surgical site infection (SSI), resulting in high risk of hernia recurrence and re-operations.[22] A feasible strategy to control SSI in the repair is the local delivery of antibiotics from a functional mesh.[23] Meshes functionalized by physical dipping/soaking or coating are commonly characterized by a burst drug release and a limited period of antibacterial protection. Furthermore, physical coating delamination during mesh handling and implantation may lead to treatment failure.[9] Creating a stable and sustained drug release system is essential for fabricating such an antibacterial mesh, in which a multigradient structure can ensure the loading efficiency and the continuous release of the drug. In this study, TEM images confirmed the physical adsorption of AMX in MWCNTs, forming the primary antibiotic releasing. When AMX@MWCNTs were monitored for 72 h in vitro, they displayed a relative burst release. After AMX@MWCNTs were grafted onto the PCL/SF mesh, they achieved sustained release of AMX through the multigradient structure. The burst release of AMX from the AMX@MWCNTs was attributed to its physical adsorption, which allowed AMX to readily desorb from the inner walls of the MWCNTs and enter the buffer solution.[24] In comparison, the molecular chains of PCL/SF–AMX@MWCNTs had to be broken to allow the separation of the AMX@MWCNTs and the subsequent release of AMX from the MWCNTs. The structure of the functional mesh makes AMX releases from an initial low-dosage, but guaranteed the long-term efficacy of antibiosis by maintaining the concentration of AMX for longer. Because the functional mesh is constructed by physical adsorption and chemical grafting, it also maintains a basic physical nanoscale structure, making it ideal for inhibiting mesh-induced inflammatory response in vivo.

After implantation, both the PCL/SF and PCL/SF–AMX@MWCNT meshes initially triggered an inflammatory response. The histological staining showed that the functional mesh with sustainable antibacterial properties induced a milder reaction, including less inflammatory cell infiltration and morphologically looser fibrous capsule formation. Implantation of mesh is commonly associated with inflammatory foreign body reaction, and the continuous incitation could make mesh postoperative adhesion and further fibrous encapsulation.[25] Within the highly orchestrated and complicated process, the inflammatory infiltration of granulocytes that characterized as CD11b$^+$ cells attenuated more prominently in the functional mesh. In the foreign body reaction, the recruitment of activated macrophages that characterized as CD68$^+$ cells underwent a similar decreasing tendency. The incited macrophages, together with the fibroblasts-dominated cells, promote the excess collagen secretion and deposition by regulating IL-10, TGF-β, and VEGF under inflammatory condition.[26] By the end of 14 days, the functional mesh had developed more collagen remodeling instead of deposition than PCL/SF mesh. It not only reflected the extent of mesh-induced inflammation by capsule thickness, but confirmed the strategies to relieve this response by combining therapeutics with mesh-designed architecture are effective in remodeling.

The host response to the biodegradable mesh, including the inflammatory response, immune rejection and incorporation, determine the ultimate effect of the repair. Despite the adding of MWCNTs could induce inflammatory and foreign body reaction, it underwent rapid, first-order clearance from the blood compartment via renal excretion and had little influence on cell proliferation within safe concentration, as we described previously.[11,27] Furthermore, the antibacterial mesh substantially induced a milder inflammatory foreign body response than non-MWCNTs containing mesh. It is expected to improve the host incorporation by allowing extracellular matrix remodeling and supporting abdominal wall defect repair with tissue-matched mechanical properties. We deem it a meaningful attempt to fabricate a functional nanofibrous mesh, and more in vivo mechanical and incorporated study of the mesh after optimizing critical parameters will be adapted to the further intraperitoneal repair in a larger animal study.

Conclusion

In this study, we fabricated a PCL/SF–AMX@MWCNT nanofibrous mesh via diverse approaches. AMX was loaded into tubular MWCNTs by physical adsorption. The AMX@MWCNTs were grafted onto electrospun PCL/SF chemically and the functional mesh was constructed by simultaneous crosslinking. The functionalization improved

the elasticity of the PCL/SF mesh to match that of the native abdominal wall, and relieved the burst release behavior of AMX, allowing sustained AMX release in vitro and subsided the inflammatory and foreign body reactions in vivo. The materials and strategies used in this study make this functional mesh a promising candidate for the repair of abdominal wall defects.

Funding

Disclosure

The authors declare no conflict of interest.

References

1. Brown CN, Finch JG. Which mesh for hernia repair? *Ann R Coll Surg Engl*. 2010;92(4):272–278. doi:10.1308/003588410X12664192076296
2. Butler CE, Burns NK, Campbell KT, et al. Comparison of cross-linked and noncross-linked porcine acellular dermal matrices for ventral hernia repair. *J Am Coll Surg*. 2010;211(3):368–376. doi:10.1016/j.jamcollsurg.2010.04.024
3. Guillaume O, Perez-Tanoira R, Fortelny R, et al. Infections associated with mesh repairs of abdominal wall hernias: are antimicrobial biomaterials the longed-for solution? *Biomaterials*. 2018;167:15–31. doi:10.1016/j.biomaterials.2018.03.017
4. Plencner M, East B, Tonar Z, et al. Abdominal closure reinforcement by using polypropylene mesh functionalized with poly-Ɛ-caprolactone nanofibers and growth factors for prevention of incisional hernia formation. *Int J Nanomedicine*. 2014;9:3263–3277. doi:10.2147/IJN.S63095
5. Gluais M, Clouet J, Fusellier M, et al. In vitro and in vivo evaluation of an electrospun-aligned microfibrous implant for annulus fibrosus repair. *Biomaterials*. 2019;205:81–93. doi:10.1016/j.biomaterials.2019.03.010
6. Ghalei S, Nourmohammadi J, Solouk A, et al. Enhanced cellular response elicited by addition of amniotic fluid to alginate hydrogel-electrospun silk fibroin fibers for potential wound dressing application. *Colloids Surf B Biointerfaces*. 2018;172:82–89. doi:10.1016/j.colsurfb.2018.08.028
7. Letouzey V, Lavigne JP, Garric X, et al. Is degradable antibiotic coating for synthetic meshes provide protection against experimental animal infection after fascia repair? *J Biomed Mater Res B Appl Biomater*. 2012;100(2):471–479. doi:10.1002/jbm.b.31973
8. Wiegering A, Sinha B, Spor L, et al. Gentamicin for prevention of intraoperative mesh contamination: demonstration of high bactericide effect (in vitro) and low systemic bioavailability (in vivo). *Hernia*. 2014;18(5):691–700. doi:10.1007/s10029-014-1293-x
9. Guillaume O, Lavigne JP, Lefranc O, et al. New antibiotic-eluting mesh used for soft tissue reinforcement. *Acta Biomater*. 2011;7 (9):3390–3397. doi:10.1016/j.actbio.2011.05.009
10. Song N, Wang MW, Jin Y, et al. Magnetic multiwalled carbon nanotubes with controlled release of epirubicin: an intravesical instillation system for bladder cancer. *Int J Nanomed*. 2019;14:1241–1254. doi:10.2147/IJN.S189688
11. Liu Z, Feng X, Wang H, et al. Carbon nanotubes as VEGF carriers to improve the early vascularization of porcine small intestinal submucosa in abdominal wall defect repair. *Int J Nanomedicine*. 2014;9:1275–1286. doi:10.2147/IJN.S58626
12. Jetbumpenkul P, Amornsudthiwat P, Kanokpanont S, et al. Balanced electrostatic blending approach: an alternative to chemical crosslinking of Thai silk fibroin/gelatin scaffold. *Int J Biol Macromol*. 2012;50 (1):7–13. doi:10.1016/j.ijbiomac.2011.08.028
13. Liechty WB, Kryscio DR, Slaughter BV, et al. Polymers for drug delivery systems. *Annu Rev Chem Biomol Eng*. 2010;1:149–173. doi:10.1146/annurev-chembioeng-073009-100847
14. Fanelli S, Zimmermann A, Totóli EG, et al. FTIR spectrophotometry as a green tool for quantitative analysis of drugs: practical application to amoxicillin. *J Chem*. 2018;2018:1–8. doi:10.1155/2018/3920810
15. Deeken CR, Lake SP. Mechanical properties of the abdominal wall and biomaterials utilized for hernia repair. *J Mech Behav Biomed Mater*. 2017;74:411–427. doi:10.1016/j.jmbbm.2017.05.008
16. Liu Z, Yang Z, Zhou Z, et al. Host tissue integration process in abdominal wall defect repair: a comparison of two porcine-derived grafts in a long-term study. *Expert Opin Biol Ther*. 2014;14 (7):883–892. doi:10.1517/14712598.2014.907783
17. Abdallah O, Jalali F, Zamani S, et al. Fabrication & characterization of 3D electrospun biodegradable nanofibers for wound dressing. drug delivery and other tissue engineering Applications. *Pharm Nanotechnol*. 2016;4 (3):191–201. doi:10.2174/2211738504666160720125322
18. Wickham A, Sjolander D, Bergstrom G, et al. Near-infrared emitting and pro-angiogenic electrospun conjugated polymer scaffold for optical biomaterial tracking. *Adv Funct Mater*. 2015;25:4274–4281. doi:10.1002/adfm.201500351
19. Kureshi A, Vaiude P, Nazhat SN, et al. Matrix mechanical properties of transversalis fascia in inguinal herniation as a model for tissue expansion. *J Biomech*. 2008;41(16):3462–3468. doi:10.1016/j.jbiomech.2008.08.018
20. Pott PP, Schwarz ML, Gundling R, et al. Mechanical properties of mesh materials used for hernia repair and soft tissue augmentation. *PLoS One*. 2012;7:e46978. doi:10.1371/journal.pone.0046978
21. Junge K, Klinge U, Prescher A, et al. Elasticity of the anterior abdominal wall and impact for reparation of incisional hernias using mesh implants. *Hernia*. 2001;5(3):113–118. doi:10.1007/s100290100019
22. Sabbagh C, Verhaeghe P, Brehant O, et al. Partial removal of infected parietal meshes is a safe procedure. *Hernia*. 2012;16(4):445–449. doi:10.1007/s10029-012-0931-4
23. Pérez-Köhler B, Bayon Y, Bellón JM. Mesh infection and hernia repair: a review. *Surg Infect*. 2016;17:124–137. doi:10.1089/sur.2015.078
24. Badakhshanian E, Hemmati K, Ghaemy M. Enhancement of mechanical properties of nanohydrogels based on natural gum with functionalized multiwall carbon nanotube: study of swelling and drug release. *Polymer*. 2016;60:282–289. doi:10.1016/j.polymer.2016.03.028
25. Heymann F, von Trotha KT, Preisinger C, et al. Polypropylene mesh implantation for hernia repair causes myeloid cell-driven persistent inflammation. *JCI Insight*. 2019;4(2):e123862. doi:10.1172/jci.insight.123862
26. Krenkel O, Tacke F. Liver macrophages in tissue homeostasis and disease. *Nat Rev Immunol*. 2017;17(5):306–321. doi:10.1038/nri.2017.11
27. Singh R, Pantarotto D, Lacerda L, et al. Tissue biodistribution and blood clearance rates of intravenously administered carbon nanotube radiotracers. *Proc Natl Acad Sci U S A*. 2006;103(9):3357–3362. doi:10.1073/pnas.0509009103